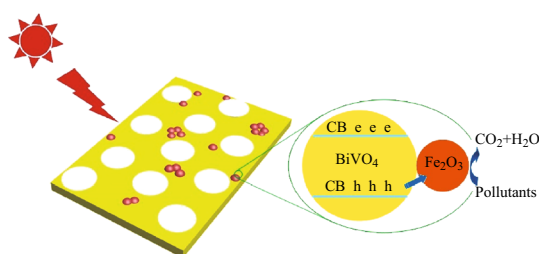ARTICLE

Fe₂O₃-Modified Porous BiVO₄ Nanoplates with Enhanced Photocatalytic Activity

Ping Cai · Shu-Mei Zhou · De-Kun Ma · Shen-Nan Liu · Wei Chen · Shao-Ming Huang

Abstract As $BiVO_4$ is one of the most popular visible-light-responding photocatalysts, it has been widely used for visible-light-driven water splitting and environmental purification. However, the typical photocatalytic activity of unmodified $BiVO_4$ for the degradation of organic pollutants is still not impressive. To address this limitation, we studied Fe_2O_3-modified porous $BiVO_4$ nanoplates. Compared with unmodified $BiVO_4$, the Fe_2O_3-modified porous $BiVO_4$ nanoplates showed significantly enhanced photocatalytic activities in decomposing both dye and colorless pollutant models, such as rhodamine B (RhB) and phenol, respectively. The pseudo-first-order reaction rate constants for the degradation of RhB and phenol on Fe_2O_3-modified $BiVO_4$ porous nanoplates are 27 and 31 times larger than that of pristine $BiVO_4$, respectively. We also found that the Fe_2O_3 may act as an efficient non-precious metal co-catalyst, which is responsible for the excellent photocatalytic activity of $Fe_2O_3/BiVO_4$.
Graphical Abstract Fe_2O_3, as a cheap and efficient co-catalyst, could greatly enhance the photocatalytic activity of $BiVO_4$ porous nanoplates in decomposing organic pollutants.

Ping Cai and Shu-Mei Zhou have contributed equally to this work.

P. Cai · S.-M. Zhou · D.-K. Ma (✉) · S.-N. Liu · W. Chen · S.-M. Huang (✉)
Nanomaterials and Chemistry Key Laboratory, Wenzhou University, Wenzhou 325027, Zhejiang, People's Republic of China
e-mail: dkma@wzu.edu.cn

S.-M. Huang
e-mail: smhuang@wzu.edu.cn

1 Introduction

As $BiVO_4$ is one of the most popular visible-light-responding photocatalysts, it has attracted much attention since Kudo and co-authors first reported its photocatalytic activity in 1998 [1]. To improve the photocatalytic activity of $BiVO_4$, some typical strategies such as preparing monoclinic crystalline phase [2], obtaining large specific surface area and high-energy facets [3, 4], constructing special architectures [5, 6], and combining two or several above methods together have been developed [7].

184

Nano-Micro Lett. (2015) 7(2):183–193

However, until now, the photocatalytic activity of single-component BiVO$_4$ is still not ideal yet for practical application. The rational design of composite photocatalysts could extend the spectral responsive range and promote the separation of photogenerated carriers and thus would improve photocatalytic activity dramatically compared to their host single-component materials [8, 9]. Based on this strategy, we fabricated n–p core–shell BiVO$_4$@Bi$_2$O$_3$ and n–n Bi$_2$S$_3$/BiVO$_4$ composite microspheres previously [10, 11]. Although these composite materials showed better photocatalytic activity than the pure BiVO$_4$, their photocatalytic activity was still not impressive. The studies on photoelectrochemical water splitting of BiVO$_4$ as photoanodes have showed that BiVO$_4$ was poor catalyst for water oxidation. However, the appropriate modification of its surface with various oxygen evolution catalysts such as cobalt–phosphate, RhO$_2$, and Pt could greatly improve its performance [12, 13]. These findings suggest that rationally loading co-catalyst on the surface of BiVO$_4$ can improve its photocatalytic activity for the degradation of various organic pollutants. Recently, Li's group reported that the photocatalytic activity of BiVO$_4$ in oxidizing thiophene could be significantly enhanced through the modification with Pt and RuO$_2$ co-catalysts [14]. Nevertheless, Pt and Ru are noble metals and expensive reagents. Therefore, it would be highly desirable if we can achieve the enhanced photocatalytic activity of BiVO$_4$ using earth-abundant elements instead of the rare and precious ones [15].

Fe$_2$O$_3$ consists of earth-abundant iron and oxygen elements and possesses the advantages of low cost, environmental friendliness and easy production, which has wide applications in many fields such as energy storage and conversion [16, 17], catalysis [18], sensing and biomedicine [19, 20]. As n-type semiconductor with a band gap of ca. 2.2 eV, Fe$_2$O$_3$ is also a potential visible-light-driven photocatalyst [21]. Nevertheless, the photocatalytic activity of unmodified Fe$_2$O$_3$ is poor because of its low carrier mobility, short minority carrier life time (ca. 10 ps) and diffusion length (ca. 2–4 nm) [22]. Therefore, there has been a lot of research focused on how to enhance photoelectrochemical and photocatalytic performance of Fe$_2$O$_3$ [23, 24]. On the other hand, the successful applications of Fe$_2$O$_3$ in many important organic catalytic reactions suggested that it had good catalytic reaction activity [18, 25]. However, to the best of our knowledge, Fe$_2$O$_3$ as a role of co-catalyst in photocatalytic system has never been reported until now.

On the other hand, the fabrication of porous two-dimensional (2D) nanostructures has drawn much interest because the porous 2D structure of these materials can increase materials' surface area, facilitate the adsorption and diffusion of reactant molecules, and accelerate the transfer of photogenerated carriers from the interior to the surface of the material [26–28]. As a result, the photocatalysts with porous 2D nanostructures are expected to have good photocatalytic activity. Recently, Yu and co-authors have reported the synthesis of porous CuS/ZnS nanosheets with excellent photocatalytic activity through cation exchange reaction between performed inorganic–organic hybrid ZnS(en)$_{0.5}$ nanosheets and Cu^{2+} ions [29]. Similarly, nanoporous Cd$_x$Zn$_{1-x}$S nanosheets have been prepared through the cation exchange reaction of ZnS–amine nanosheets with cadmium ions [30]. However, the above-mentioned methods were limited in a few inorganic–organic hybrid 2D nanomaterials. Comparatively speaking, 2D metal complex nanostructures are more easily prepared through self-assembly of ligand at room temperature, which is driven by various non-covalent interactions including π–π stacking, van der Waals bonding, hydrophobic interactions, etc. [31–33]. Subsequently, 2D porous compounds nanostructures can be obtained by exchange reaction between ligands in 2D metal complexes nanostructures and anions in the desired compounds under certain conditions. However, this kind of ligand-anion exchange route to synthesize 2D porous nanostructured material has not, so far, been developed.

In this study, we present a new method for synthesizing porous BiVO$_4$ nanoplates via exchange reaction between ligand 1,4-benzenedicarboxylate (BDC) in 2D Bi$_2$(BDC)$_3$ nanoplates derived from direct self-assembly and VO$_4^{3-}$ anions under hydrothermal condition, schematically shown in Fig. 1. Subsequently, Fe$_2$O$_3$-modified porous BiVO$_4$ nanoplates were obtained through a simple hydrothermal deposition–precipitation route. The as-obtained Fe$_2$O$_3$/BiVO$_4$ products displayed excellent photocatalytic activities for degrading both dye and colorless organic pollutants. Based on UV–Visible diffuse-reflectance spectra (DRS), photoluminescence (PL) spectra, and a series of comparative experiments, Fe$_2$O$_3$ as a role of non-precious metal co-catalyst in the present composite system was proposed.

2 Experimental Section

2.1 Preparation of Porous BiVO$_4$ Nanoplates

Bi$_2$(BDC)$_3$ nanoplates were prepared through our previous report [34]. For the preparation of porous BiVO$_4$ nanoplates, 0.1504 g of the as-obtained Bi$_2$(BDC)$_3$ and 0.0732 g of NaVO$_3$ were dispersed into 40 mL of ultrapure water under stirring. Then the solution was put into a Teflon® lined stainless steel autoclave with 50 mL of capability and heated at 180 °C for 10 h. After the autoclave was cooled to room temperature, the products were separated through centrifugation and washed three times with ultrapure water and absolute ethanol. Finally, the products were dried under vacuum at 60 °C for 4 h.
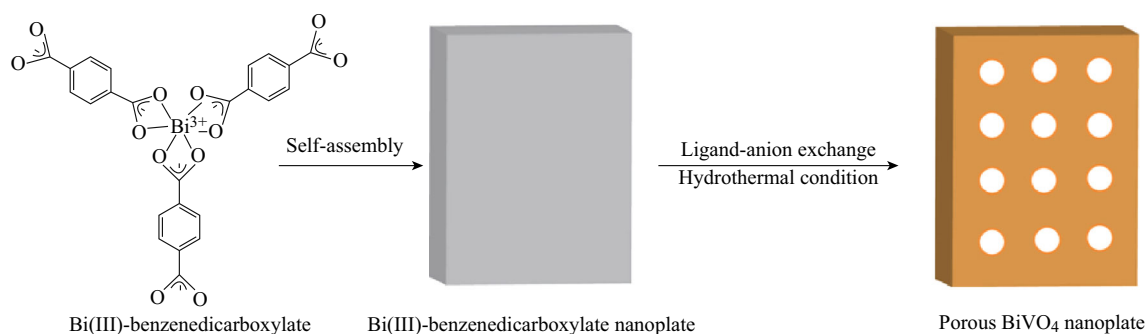
Fig. 1 Representation for the synthetic route to porous BiVO$_4$ nanoplate

2.2 Preparation of Fe$_2$O$_3$-Modified BiVO$_4$ Porous Nanoplates

In a typical procedure, 0.4 mmol of porous BiVO$_4$ nanoplates, 1.0 mmol of NaOH, and different amounts of Fe(NO$_3$)$_3$ (0.008, 0.02, 0.04 mmol) were added into 40 mL of ultrapure water in sequence under stirring. After that, the solution was put into a Teflon$^®$ lined stainless steel autoclave with 50 mL of capability and heated at 160 °C for 12 h. After the autoclave was cooled to room temperature, the resultant products were separated via centrifugation and washed three times with ultrapure water and absolute ethanol, respectively. Finally, the products were dried under vacuum at 60 °C for 4 h.

2.3 Characterizations

Powder X-ray diffraction (XRD) patterns were carried out on a Bruker D8 Advanced X-ray diffractometer using Cu Kα radiation ($\lambda = 0.15418$ nm) at a scanning rate of 8°/min in the 2θ range of 10°–70°. X-ray photoelectron spectroscopy (XPS) measurements were carried out with a Thermo ESCALAB 250 X-ray photoelectron spectrometer with an excitation source of Al Kα radiation ($\lambda = 1,253.6$ eV). Field emission scanning electron microscopy (FE-SEM) images and energy dispersed X-ray (EDX) spectra were taken on a Nova NanoSEM 200 scanning electron microscope. Transmission electron microscopy (TEM), EDX, high-resolution TEM (HRTEM) images and mapping images were taken on a JEOL 2010 microscope, using an accelerating voltage of 200 kV. The UV–Visible DRS were recorded on a UV2450 (Shimadzu) using BaSO$_4$ as reference. The PL spectra were recorded on a Fluoromax-4 spectrofluorometer (HORIBA Jobin Yvon Inc.) equipped with a 150 W xenon lamp as the excitation source.

2.4 Photocatalytic Properties

The photocatalytic activity of Fe$_2$O$_3$/BiVO$_4$ nanoplates was evaluated by the degradation of RhB and phenol under visible-light irradiation from 500 W Xe light (CHF-XM500, purchased from Beijing Trusttech Co., Ltd) equipped with a 400 nm cutoff filter, and water splitting using a 300 W Xe lamp and optical cutoff filter ($\lambda > 420$ nm). In a typical process, 100 mg of photocatalysts was added to 100 mL of rhodamine B (RhB) solution (10^{-5} mol L^{-1}). Before illumination, the solution was magnetically stirred in the dark for 12 h to ensure an adsorption–desorption equilibrium between the photocatalysts and RhB. After that, the solution was exposed to visible light irradiation under magnetic stirring. At given time intervals, 3 mL of solution was sampled and centrifuged to remove the photocatalyst particles. Then, the filtrates were analyzed by recording variations of the absorption band maximum (553 nm) in the UV–Vis spectra of RhB by using a Shimadzu UV2501PC spectrophotometer. The studies of photocatalytic activities for other samples adopted the same measurement process. For photocatalytic degradation of phenol, the initial concentration of phenol solution was 1×10^{-4} mol L^{-1} and kept other conditions unchanged. After visible light irradiation of different period time, the centrifugated solution was analyzed by recording variations of the absorption band maximum (270 nm) of phenol in the UV–Vis spectra by using a Shimadzu UV2450 PC spectrophotometer. As to photocatalytic water splitting, 0.1 g of photocatalysts was dispersed in 150 mL of 0.02 M aqueous AgNO$_3$ solution in a Pyrex reaction cell and thoroughly degassed by evacuation in order to drive off the air inside. The amount of evolved O$_2$ was measured by an online gas chromatograph.

3 Results and Discussion

3.1 Crystal Structure, Compositions and Morphology

Figure 2a shows XRD pattern of the products obtained through the direct exchange reaction of BDC molecules in Bi$_2$(BDC)$_3$ with VO$_4$$^{3-}$ anions under hydrothermal condition. All the diffraction peaks can be indexed to a monoclinic scheelite structure of BiVO$_4$ (JCPDS No.

186

Nano-Micro Lett. (2015) 7(2):183–193

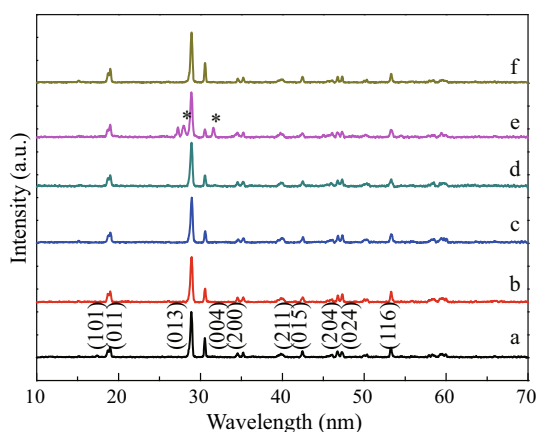**Fig. 2** XRD patterns of the products hydrothermally synthesized with $Bi_2(BDC)_3$ and $NaVO_3$ *a* $BiVO_4$, *b* NaOH and 0.008, *c* NaOH and 0.02, *d* NaOH and 0.04, *e* NaOH and 0 mmol of $Fe(NO_3)_3$, respectively, and *f* $BiVO_4$ and $Fe(NO_3)_3$

75-2480). No obvious reflection peaks from other impurities can be observed. When only 1 mmol of NaOH were used, some part of $BiVO_4$ could be converted into Bi_2O_3 (Fig. 2e, marked with asterisks) and formed $Bi_2O_3/BiVO_4$ composites under hydrothermal treatment, which is consistent with our previous report [10]. But when different amounts of $Fe(NO_3)_3$ (0.008, 0.02, 0.04 mmol) and 1 mmol of NaOH were simultaneously added into the reaction system, the resultant products contained no Bi_2O_3 (Fig. 2b, c, d). The results showed that Fe^{3+} ions would preferentially react with OH^- ions in solution. But, no diffraction peaks of Fe_2O_3 could be observed because its content in the products is lower than the XRD limit of detection and/or poor crystalline degree. The existence of Fe_2O_3 could be confirmed by subsequent XPS, EDX spectra, and HRTEM images.

The survey XPS spectrum reveals that the products are composed of Bi, V, O, Fe, and C elements (Supporting Information, Fig. S1). Figure 3a, b, c and d shows high-resolution XPS spectra of Bi 4f, V 2p, Fe 2p, and O 1s of the products, respectively. In Fig. 3a, the peaks with binding energies of 159.2 and 164.4 eV correspond to Bi 4f7/2 and Bi 4f5/2 in $BiVO_4$ [11], respectively. The values (516.7 and 524.5 eV) of the binding energies for V 2p are in agreement with previous report on V^{5+} in $BiVO_4$ [35]. In the high-resolution Fe 2p spectrum (Fig. 3c), two distinct peaks located at 710.8 eV for Fe 2p3/2 and 724.2 eV for Fe 2p1/2 with a shake-up satellite at 719.3 eV were observed. This is characteristic of Fe^{3+} in Fe_2O_3 [19]. The O 1s peak is asymmetric, indicating that different oxygen species were present in the near surface region. The major component is attributed to the lattice oxygen (529.8 eV) in $BiVO_4$ or Fe_2O_3. The second component centered at 532.3 eV is associated with non-equivalent OH group on the surface [36]. Combined with the XRD results, it can be

known that the products consist of $BiVO_4$ and possible Fe_2O_3.

We chose $Bi_2(BDC)_3$ as precursor to synthesize $BiVO_4$ because the former was easily self-assembled into nanostructures through π–π stacking of benzene ring structure in BDC molecule at room temperature. Moreover, the flexible BDC ligand was helpful to alleviate the strain caused by crystal lattice mismatch between $Bi_2(BDC)_3$ and $BiVO_4$ and maintain the framework of nanoplate during chemical conversion process. Figure 4a represents a typical FE-SEM image of the as-obtained $Bi_2(BDC)_3$ precursor, which shows that the sample is nanoplates with average size of 100 nm in thickness, 500 nm in width, and 1.5 μm in length. After chemical transformation, $Bi_2(BDC)_3$ nanoplates were converted into porous $BiVO_4$ nanoplates (Fig. 4b). These pores are linked together and distributed throughout the whole nanoplates. Magnified FE-SEM image shows that there are some tiny nanoparticles on the surfaces of the products obtained through hydrothermal deposition–precipitation route (Fig. S2). Further insight morphology and the microstructure of the products can be obtained from TEM and HRTEM images. In agreement with FE-SEM observations, TEM also shows that the products are porous nanoplates. Careful analyses show that there are some aggregates of tiny particles (marked with white arrowhead) closely integrating with the surfaces of nanoplates. Figure 4d represents HRTEM image recorded on the white rectangular area in Fig. 4c. The fringe spacing of 0.362 and 0.312 nm in the HRTEM image corresponds to the interplanar separation of (110) and (103) planes of monoclinic $BiVO_4$, respectively. The HRTEM image of tiny particles displays the fringe spacing of 0.221 nm, which is consistent with the interplanar spacing of (113) plane of hexagonal-phase Fe_2O_3. The EDX spectroscopy recorded on a single nanoplate shows that the sample consists of Bi, V, Fe, Cu, C, and O elements (Fig. 4f). The Cu and C elements come from copper grid coated carbon for sample support. Bi, V, Fe and O elements correspond to $BiVO_4$ and Fe_2O_3. The EDX spectrum further supports the results of HRTEM. The mapping images of an individual $Fe_2O_3/BiVO_4$ porous nanoplate show that Fe_2O_3 nanoparticles scattered unequally on the surfaces of porous $BiVO_4$ nanoplates (Fig. S3). The quantitative calculation on the EDX spectrum recorded on SEM (Fig. S4) shows that the content of Fe_2O_3 in the sample is *c*a. 3.8 mol %. All the above results indicate that the as-obtained products are Fe_2O_3-modified $BiVO_4$ porous nanoplates.

3.2 Photocatalytic Properties

The photocatalytic activities of the as-obtained $Fe_2O_3/BiVO_4$ porous nanoplates were evaluated by the degradation of RhB and phenol, common pollutant models as dye

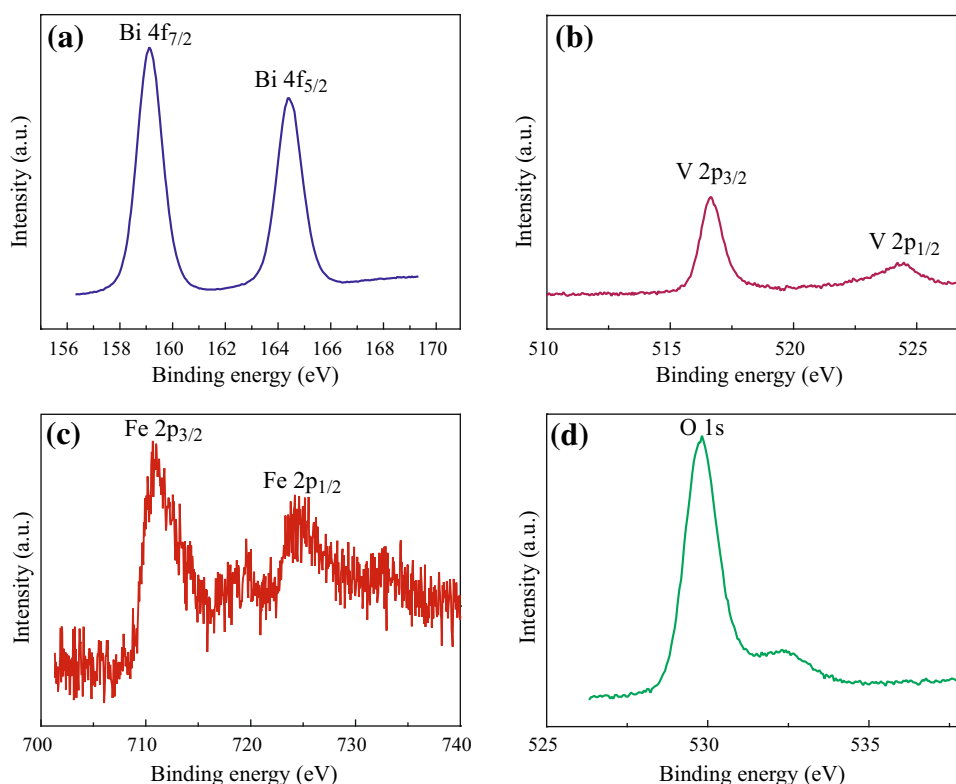**Fig. 3** Typical XPS high-resolution spectra of the products synthesized with BiVO$_4$, NaOH, and 0.02 mmol of Fe(NO$_3$)$_3$: **a** Bi 4f, **b** V 2p, **c** Fe 2p, and **d** O 1 s

and colorless organic compounds, respectively, in water under visible light irradiation ($\lambda > 400$ nm). As shown in Fig. 5a, the photodegradation efficiency of RhB over Fe$_2$O$_3$/BiVO$_4$ is near 100 % within 80 min under visible light irradiation. However, RhB is stable and has a negligible degradation in the absence of any photocatalysts under visible light irradiation [37]. The photocatalytic activity of Fe$_2$O$_3$/BiVO$_4$ is significantly superior to pristine BiVO$_4$ and Bi$_2$O$_3$/BiVO$_4$ as well. Considering most of the photocatalytic reactions follow a pseudo-first-order kinetic equation: $\ln(C_0/C) = kt$ (where C_0 and C are the equilibrium concentration of adsorption and the concentration of RhB at the irradiation time t, respectively, and k is the apparent rate constant), the plots of $\ln(C_0/C)$ versus t were performed. The $\ln(C_0/C)$ versus t displays a linear relationship (Fig. 5b), which shows that the photodegradation of RhB on these photocatalysts obeys the rules of first-order reaction kinetics. From the fitting results, the apparent reaction rate constants are 0.0013, 0.0057, and 0.0358 min^{-1} for pristine BiVO$_4$, Bi$_2$O$_3$/BiVO$_4$, and Fe$_2$O$_3$/BiVO$_4$, respectively. As a result, the photocatalytic reaction rate of Fe$_2$O$_3$/BiVO$_4$ is 27 and 6 times larger than that of pristine BiVO$_4$ and Bi$_2$O$_3$/BiVO$_4$, respectively. Fe$_2$O$_3$/BiVO$_4$ also displayed excellent photocatalytic

activity for degrading colorless phenol. As shown in Fig. 5c, the photocatalytic activity of BiVO$_4$ was greatly enhanced after the modification of Fe$_2$O$_3$, which was in good agreement with the results of photocatalytic decomposition of RhB. The apparent reaction rate constants are 0.0006, 0.0009, and 0.019 min^{-1} for BiVO$_4$, Bi$_2$O$_3$/BiVO$_4$, and Fe$_2$O$_3$/BiVO$_4$, respectively. As a result, the photocatalytic reaction rate of Fe$_2$O$_3$/BiVO$_4$ is 31 and 21 times larger than that of unmodified BiVO$_4$ and Bi$_2$O$_3$/BiVO$_4$, respectively. Whether the pollutant model is RhB or phenol, the amount of Fe$_2$O$_3$ in the products has obvious influence on photocatalytic activity of Fe$_2$O$_3$/BiVO$_4$. When too lower or too higher concentration of Fe(NO$_3$)$_3$ was used, less or more Fe$_2$O$_3$ was produced. It was found that the photocatalytic activity of Fe$_2$O$_3$/BiVO$_4$ would decline in both cases. However, all the composites show higher photocatalytic activity than pure BiVO$_4$. Therefore, finely adjusting the content of Fe$_2$O$_3$ will further improve the photocatalytic activity of Fe$_2$O$_3$/BiVO$_4$. In addition, Fe$_2$O$_3$-modified BiVO$_4$ porous nanoplates show good reusability (Fig. 6). After five times cycles for the photocatalytic degradation of RhB and phenol, the sample did not exhibit obvious loss of photocatalytic activity.
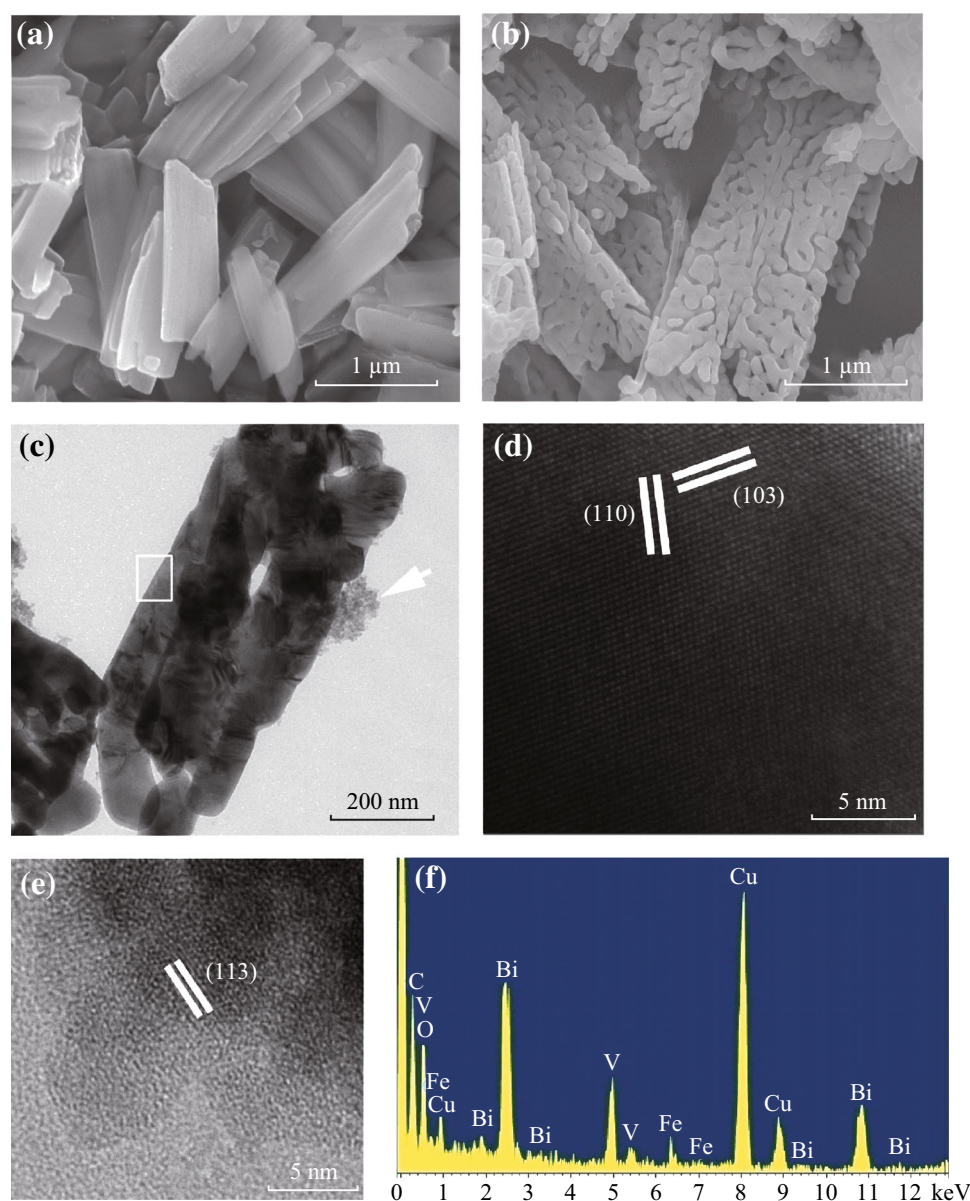
Fig. 4 FE-SEM images of **a** $Bi_2(BDC)_3$ and **b** $BiVO_4$. **c** TEM image of Fe_2O_3-modified $BiVO_4$. HRTEM images recorded on the places marked with *white rectangular area* **d** and *white arrowhead* **e** in Fig. 4c. **f** EDX spectrum performed on a single nanoplate

3.3 The Role of Fe_2O_3 and Photocatalysis Mechanism

The doping of Fe^{3+} ions in the lattice of some photocatalysts or its graft on the surfaces of certain photocatalysts would enhance the photocatalytic activities of the photocatalysts [38, 39]. In order to survey whether the enhancement of photocatalytic activity of $BiVO_4$ stems from the doping or grafting effect of Fe^{3+} ions, the control experiment without using NaOH was carried out. The photocatalytic activities of the resultant products have no obvious change for the decomposition of RhB (Fig. 5a), compared with pristine $BiVO_4$. The result shows that the doping and grafting of Fe^{3+} ions were not main reasons for

the enhanced photocatalytic activity of $Fe_2O_3/BiVO_4$. Previous studies indicated that single-component Fe_2O_3 nanocrystals showed poor and negligible photocatalytic activity for the degradation of RhB and phenol under visible light irradiation [40, 41], respectively. To further understand the role of Fe_2O_3 in the composite material, Fe_2O_3 nanorods were synthesized through modified method (Supporting Information, Fig. S5 and Fig. S6) [40]. As shown in Fig. 5a and c, only a small quantity (<25 %) of RhB molecules were degraded on Fe_2O_3 nanorods within 90 min while almost no detectable decomposition was observed for phenol. It was observed that the size of Fe_2O_3 is very small in $Fe_2O_3/BiVO_4$ composites. In order to

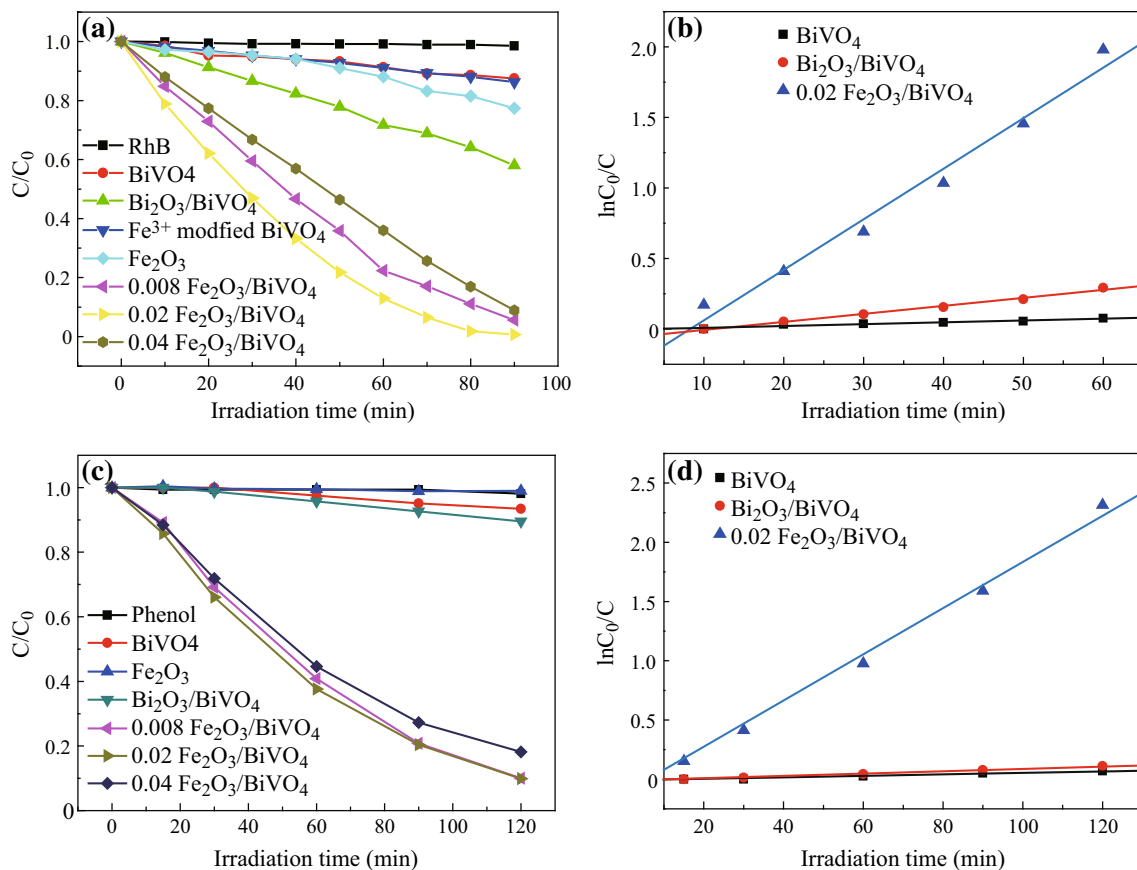**Fig. 5** **a** RhB concentration changes with irradiation time over no catalysts, $BiVO_4$, Fe^{3+} ions modified $BiVO_4$, Fe_2O_3 nanorods, $Bi_2O_3/BiVO_4$, and $Fe_2O_3/BiVO_4$ synthesized with different amounts of $Fe(NO_3)_3$. **b** Plots of $\ln(C_0/C)$ versus t of $BiVO_4$, $Bi_2O_3/BiVO_4$ and $Fe_2O_3/BiVO_4$. **c** Phenol concentration changes with irradiation time over no catalysts, Fe_2O_3 nanorods, $BiVO_4$, $Bi_2O_3/BiVO_4$, and $Fe_2O_3/BiVO_4$ synthesized with different amounts of $Fe(NO_3)_3$. **d** Plots of $\ln(C_0/C)$ versus irradiation time (t) of $BiVO_4$, $Bi_2O_3/BiVO_4$ and $Fe_2O_3/BiVO_4$. 0.008, 0.04 and 0.02 represent the amount of $Fe(NO_3)_3$ used (the unit is mmol)
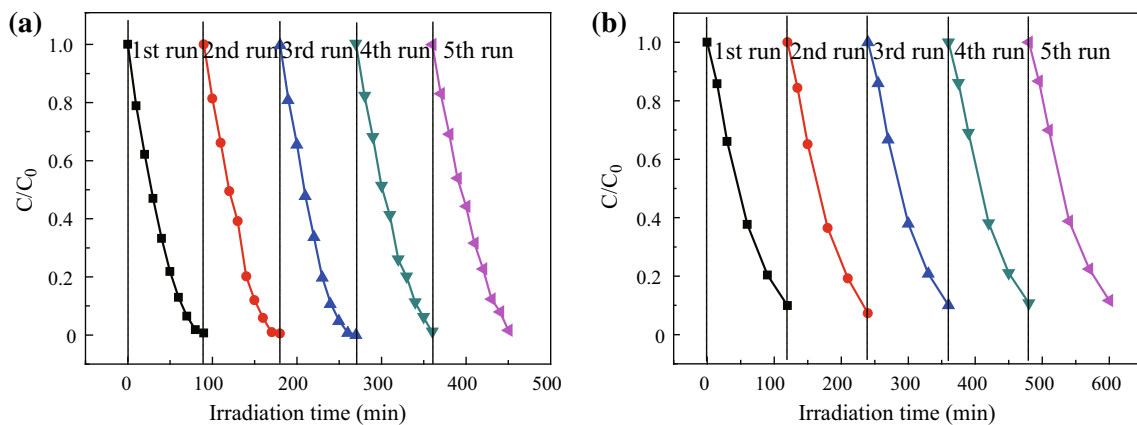

Fig. 6 The stability of Fe_2O_3 modified $BiVO_4$ porous nanoplates after 5 cycles for photocatalytic degradation of RhB (**a**) and phenol (**b**)

exclude the possibility of nanosize effect of Fe_2O_3 for the enhanced photocatalytic activity, ultrasmall Fe_2O_3 nanoparticles supported by SiO_2 nanospheres were synthesized and their photocatalytic activities were evaluated

by the degradation of phenol (Fig. S7–S9). As shown in Fig. S9, Fe_2O_3/SiO_2 showed very poor photocatalytic activity as well. The above results further indicate that Fe_2O_3 itself has very weak photocatalytic activity, which cannot
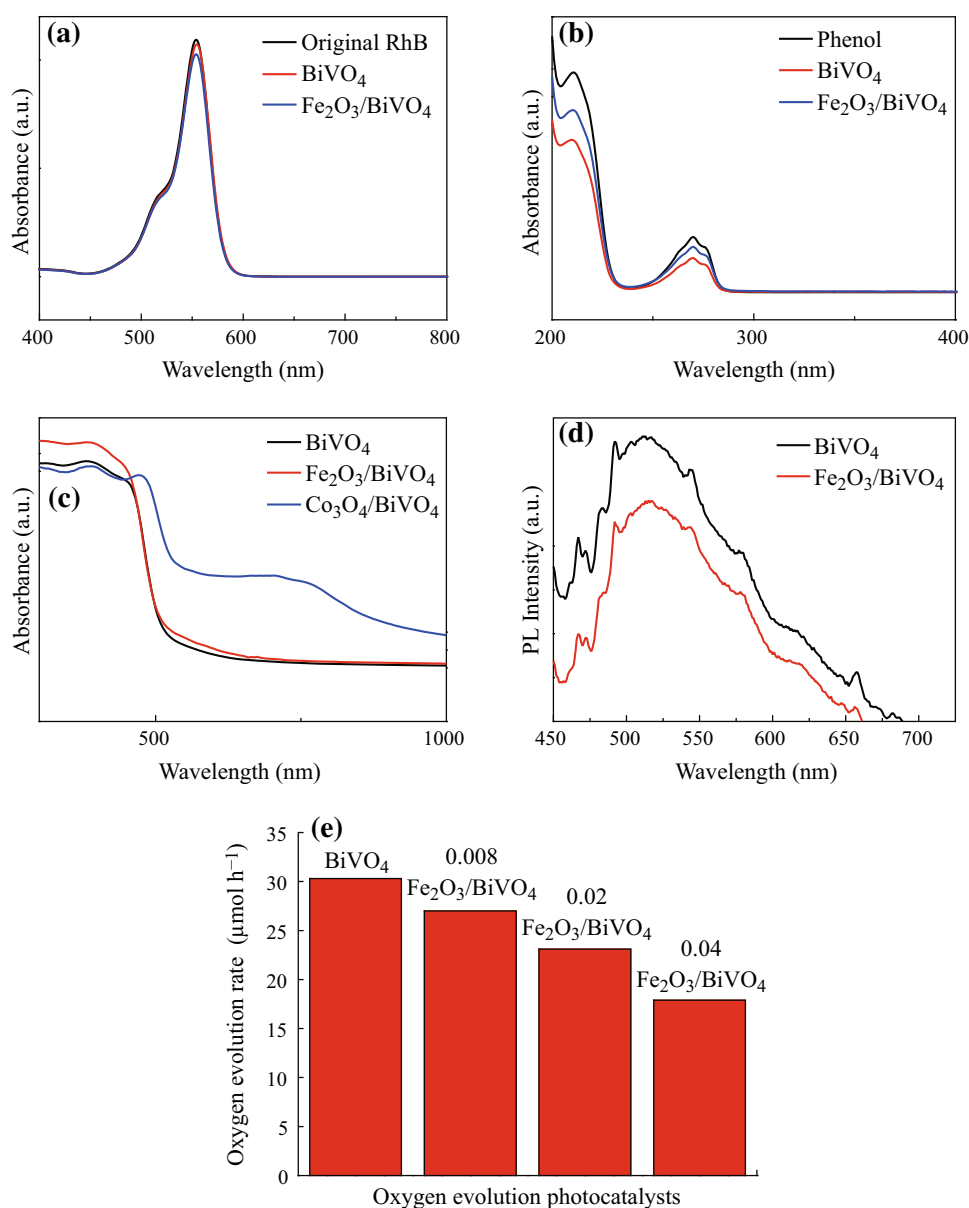
190

Nano-Micro Lett. (2015) 7(2):183–193

Fig. 7 The adsorption behavior of **a** RhB and **b** phenol on BiVO$_4$ and Fe$_2$O$_3$/BiVO$_4$. **c** UV–Vis DRS of pristine BiVO$_4$, Fe$_2$O$_3$/BiVO$_4$ and Co$_3$O$_4$/BiVO$_4$. **d** PL spectra of BiVO$_4$ and Fe$_2$O$_3$/BiVO$_4$ excited at $\lambda = 400$ nm at room temperature. **e** The oxygen evolution rate of pure BiVO$_4$, 0.008 Fe$_2$O$_3$/BiVO$_4$, 0.02 Fe$_2$O$_3$/BiVO$_4$, and 0.04 Fe$_2$O$_3$/BiVO$_4$ under visible light irradiation ($\lambda > 420$ nm)

account for the excellent photocatalytic activity in the present Fe$_2$O$_3$/BiVO$_4$ system.

The photocatalytic activity of the composite photocatalysts in decomposing organic pollutant is closely related to their adsorption capability, light energy utilization, separation efficiency of photogenerated carriers, and surface catalytic performance [42–45]. Fe$_2$O$_3$/BiVO$_4$ and pristine BiVO$_4$ have similar adsorption behavior to both RhB and phenol (Fig. 7a, b). The introduction of Fe$_2$O$_3$ and Bi$_2$O$_3$ do not noticeably improve adsorption ability of BiVO$_4$ to the organic pollutants (Fig. S10). Figure 7c represents UV–Vis DRS of Fe$_2$O$_3$/BiVO$_4$ and pristine

BiVO$_4$. There are no obvious differences between them except that Fe$_2$O$_3$/BiVO$_4$ displays slightly higher absorption in both UV and visible light region than BiVO$_4$, which is possibly attributed to larger absorption coefficient of Fe$_2$O$_3$ (ca. 10^5 cm^{-1}) than that of BiVO$_4$ and its narrower band gap (2.2 eV) [46]. As we know, PL spectra can be used as an efficient means to evaluate the separation efficiency of the photogenerated carriers [11]. Figure 7d displays the room temperature PL emission spectra (excited at 400 nm) of pure BiVO$_4$ and Fe$_2$O$_3$/BiVO$_4$. The result shows that PL emission intensity of original BiVO$_4$ decreases after it was combined with Fe$_2$O$_3$, which suggests
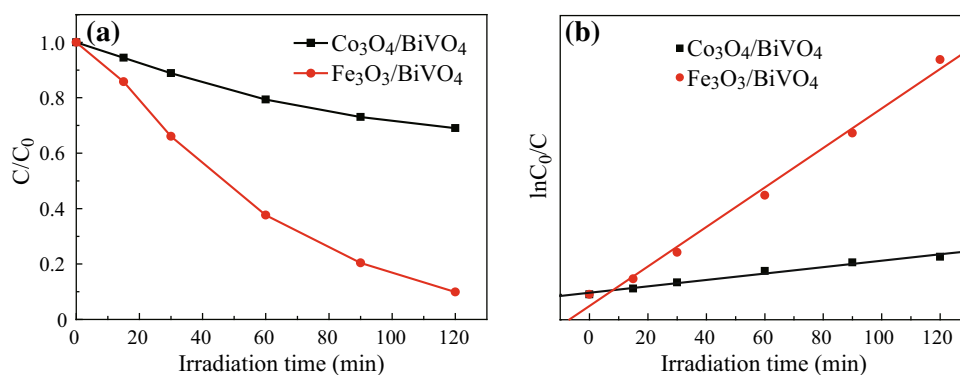
Fig. 8 **a** Phenol concentration changes with irradiation time over $Co_3O_4/BiVO_4$ and $Fe_2O_3/BiVO_4$. **b** Plots of $\ln(C_0/C)$ versus t of $Co_3O_4/BiVO_4$ and $Fe_2O_3/BiVO_4$

the photogenerated electrons and holes are efficiently separated. In order to further understand how photogenerated electron and hole migrate, the photocatalytic activities for water splitting of pure $BiVO_4$, $0.008Fe_2O_3/BiVO_4$, $0.02Fe_2O_3/BiVO_4$, and $0.04Fe_2O_3/BiVO_4$ were comparatively studied. The amount of O_2 evolved in the first hour was evaluated. As shown in Fig. 7e, the photocatalytic O_2 evolution activities of the samples gradually decline with increasing content of Fe_2O_3 and pure $BiVO_4$ possesses the best performance. The results suggest that photogenerated holes not electrons were transferred to the surfaces of Fe_2O_3. Otherwise, more O_2 will be produced on $Fe_2O_3/BiVO_4$ because the composite material can more efficiently separate photogenerated carriers than pure $BiVO_4$. $Fe_2O_3/BiVO_4$ showed lower photocatalytic water splitting activity than pure $BiVO_4$ because Fe_2O_3 had lower oxidation potential than $BiVO_4$. When photogenerated holes were transferred to the surfaces of Fe_2O_3, their water oxidation performance correspondingly weakened. The tradeoff between the separation of carriers and decreased oxidation potential leads to declined photocatalytic water splitting performance of $Fe_2O_3/BiVO_4$. Therefore, Fe_2O_3 can act as a hole scavenger and efficiently separates photogenerated carriers.

It is known that noble metals can act as co-catalysts on the surfaces of photocatalysts, which can greatly enhance the surface catalytic activity of the materials. Recent studies showed that some non-precious metal such as MoS_2, graphene, and cobalt phosphate could serve as co-catalysts like noble metal as well [47–49]. In this study, the loading of small amounts of Fe_2O_3 also enhanced surface catalytic activity of $BiVO_4$. To further support the role of a co-catalyst of Fe_2O_3 in our system, we compared the photocatalytic activity of $Fe_2O_3/BiVO_4$ and $Co_3O_4/BiVO_4$ in degrading phenol. $Co_3O_4/BiVO_4$ was prepared following reported procedures [50], where $Co_3O_4/BiVO_4$ possessed excellent photocatalytic activity for degrading phenol. As

shown in Fig. 8, the photocatalytic activity of the present $Fe_2O_3/BiVO_4$ greatly surpassed that of $Co_3O_4/BiVO_4$. The photocatalytic reaction rate constant of the former (1.9×10^{-2} min^{-1}) is six times larger than that of the latter (3×10^{-3} min^{-1}). Compared with $Fe_2O_3/BiVO_4$, $Co_3O_4/BiVO_4$ shows much larger and wider absorption in both UV and visible light region, as shown in Fig. 7c. PL spectrum indicates that the emission intensity of $BiVO_4$ was greatly reduced after the loading of Co_3O_4 (Fig. S11), which showed that photogenerated carriers were efficiently separated in $Co_3O_4/BiVO_4$ system as well. In addition, $Co_3O_4/BiVO_4$ and $Fe_2O_3/BiVO_4$ has similar adsorption ability to phenol (Fig. S12). Considering all above facts, it can be understood that higher surface catalytic activity of $Fe_2O_3/BiVO_4$ lead to its higher catalytic activity than $Co_3O_4/BiVO_4$. Specifically, Fe_2O_3 played a key role as co-catalyst for enhanced photocatalytic activity of $Fe_2O_3/BiVO_4$ due to its low content, efficient separation of photogenerated carriers and good surface catalytic activity. It should be highlighted here that the photocatalytic activity of the as-obtained $Fe_2O_3/BiVO_4$ is among one of the best photocatalysts reported to date, and is superior to noble metal Pt loaded the same porous $BiVO_4$ nanoplates (Only 40 % of phenol was degraded under the same conditions, Fig. S13).

4 Conclusions

In conclusion, $Fe_2O_3/BiVO_4$ nanoplates with porous structures have been prepared through a mild chemical conversion and subsequently hydrothermal deposition–precipitation routes. The as-prepared $Fe_2O_3/BiVO_4$ showed excellent photocatalytic activity in degrading both RhB and phenol. After the modification of Fe_2O_3, the photocatalytic activity of pristine $BiVO_4$ could be increased more than one order of magnitude. It is believed that Fe_2O_3 acts as an

efficient co-catalyst, which contributes to the excellent photocatalytic activity of $Fe_2O_3/BiVO_4$ porous nanoplates. The facile preparation method, low cost of raw materials, excellent photocatalytic activity, and good reusability of the $Fe_2O_3/BiVO_4$ porous nanoplates make the material a promising photocatalyst for the application in the field of environmental remedy.

References

1. A. Kudo, K. Ueda, H. Kato, I. Mikami, Photocatalytic O_2 evolution under visible light irradiation on $BiVO_4$ in aqueous $AgNO_3$ solution. Catal. Lett. **53**(3–4), 229–230 (1998). doi:10.1023/A:1019034728816

2. Y.F. Sun, B.Y. Qu, Q. Liu, S. Gao, Z.X. Yan, W.S. Yan, B.C. Pan, S.Q. Wei, Y. Xie, Highly efficient visible-light-driven photocatalytic activities in synthetic ordered monoclinic $BiVO_4$ quantum tubes-graphene nanocomposites. Nanoscale **4**(12), 3761–3767 (2012). doi:10.1039/c2nr30371j

3. X.F. Zhang, L.L. Du, H. Wang, X.L. Dong, X.X. Zhang, C. Ma, H.C. Ma, Highly ordered mesoporous $BiVO_4$: controllable ordering degree and super photocatalytic ability under visible light. Microporous Mesoporous Mater. **173**, 175–180 (2013). doi:10.1016/j.micromeso.2013.02.029

4. G.C. Xi, J.H. Ye, Synthesis of bismuth vanadate nanoplates with exposed 001 facets and enhanced visible-light photocatalytic properties. Chem. Commun. **46**(11), 1893–1895 (2010). doi:10.1039/b923435g

5. M. Zhou, H.B. Wu, J. Bao, L. Liang, X.W. Lou, Y. Xie, Ordered macroporous $BiVO_4$ architectures with controllable dual porosity for efficient solar water splitting. Angew. Chem. Int. Ed. **52**(33), 8579–8583 (2013). doi:10.1002/anie.201302680

6. D.N. Ke, T.Y. Peng, L. Ma, P. Cai, K. Dai, Effects of hydrothermal temperature on the microstructures of $BiVO_4$ and its photocatalytic O_2 evolution activity under visible light. Inorg. Chem. **48**(11), 4685–4691 (2009). doi:10.1021/ic900064m

7. H.Y. Jiang, X. Meng, H.X. Dai, J.G. Deng, Y.X. Liu, L. Zhang, Z.X. Zhao, R.Z. Zhang, High-performance porous spherical or octapod-like single-crystalline $BiVO_4$ photocatalysts for the removal of phenol and methylene blue under visible-light illumination. J. Hazard. Mater. **217**, 92–99 (2012). doi:10.1016/j.jhazmat.2012.02.073

8. D.Q. Zhang, G.S. Li, H.X. Li, Y.F. Lu, The development of better photocatalysts through composition- and structure-engineering. Chem.-Asian J. **8**(1), 26–40 (2013). doi:10.1002/asia.201200123

9. X.H. Gao, H.B. Wu, L.X. Zheng, Y.J. Zhong, Y. Hu, X.W. Lou, Formation of mesoporous heterostructured $BiVO_4/Bi_2S_3$ hollow discoids with enhanced photoactivity. Angew. Chem. Int. Ed. **53**(23), 5917–5921 (2014). doi:10.1002/anie.201403611

10. M.L. Guan, D.K. Ma, S.W. Hu, Y.J. Chen, S.M. Huang, From hollow olive-shaped $BiVO_4$ to n-p core-shell $BiVO_4@Bi_2O_3$ microspheres: controlled synthesis and enhanced visible-light-responsive photocatalytic properties. Inorg. Chem. **50**(3), 800–805 (2011). doi:10.1021/ic101961z

11. D.K. Ma, M.L. Guan, S.S. Liu, Y.Q. Zhang, C.W. Zhang, Y.X. He, S.M. Huang, Controlled synthesis of olive-shaped $Bi_2S_3/BiVO_4$ microspheres through a limited chemical conversion route and enhanced visible-light-responding photocatalytic activity. Dalton Trans. **41**(18), 5581–5586 (2012). doi:10.1039/c2dt30099k

12. S.K. Pilli, T.E. Furtak, L.D. Brown, T.G. Deutsch, J.A. Turner, A.M. Herring, Cobalt-phosphate (Co-Pi) catalyst modified Mo-doped $BiVO_4$ photoelectrodes for solar water oxidation. Energy Environ. Sci. **4**(12), 5028–5034 (2011). doi:10.1039/c1ee02444b

13. Y. Park, K.J. McDonald, K.S. Choi, Progress in bismuth vanadate photoanodes for use in solar water oxidation. Chem. Soc. Rev. **42**(6), 2321–2337 (2013). doi:10.1039/c2cs35260e

14. F. Lin, D.E. Wang, Z.X. Jiang, Y. Ma, J. Li, R.G. Li, C. Li, Photocatalytic oxidation of thiophene on $BiVO_4$ with dual co-catalysts Pt and RuO_2 under visible light irradiation using molecular oxygen as oxidant. Energy Environ. Sci. **5**(4), 6400–6406 (2012). doi:10.1039/c1ee02880d

15. J. Wang, X.K. Xin, Z.Q. Lin, Cu_2ZnSnS_4 nanocrystals and graphene quantum dots for photovoltaics. Nanoscale **3**(8), 3040–3048 (2011). doi:10.1039/c1nr10425j

16. L. Zhang, H.B. Wu, S. Madhavi, H.H. Hng, X.W. Lou, Formation of Fe_2O_3 microboxes with hierarchical shell structures from metal-organic frameworks and their lithium storage properties. J. Am. Chem. Soc. **134**(42), 17388–17391 (2012). doi:10.1021/ja307475c

17. B. Klahr, S. Gimenez, F. Fabregat-Santiago, T. Hamann, J. Bisquert, Water oxidation at hematite photoelectrodes: the role of surface states. J. Am. Chem. Soc. **134**(9), 4294–4302 (2012). doi:10.1021/ja210755h

18. R.V. Jagadeesh, A.E. Surkus, H. Junge, M.M. Pohl, J. Radnik, J. Rabeah, H.M. Huan, V. Schuenemann, A. Brueckner, M. Beller, Nanoscale Fe_2O_3-based catalysts for selective hydrogenation of nitroarenes to anilines. Science **342**(6162), 1073–1076 (2013). doi:10.1126/science.1242005

19. X.L. Hu, J.C. Yu, J.M. Gong, Q. Li, G.S. Li, Alpha-Fe_2O_3 nanorings prepared by a microwave-assisted hydrothermal process and their sensing properties. Adv. Mater. **19**(17), 2324–2329 (2007). doi:10.1002/adma.200602176

20. P. Tartaj, M.P. Morales, T. Gonzalez-Carreno, S. Veintemillas-Verdaguer, C.J. Serna, The iron oxides strike back: from biomedical applications to energy storage devices and photoelectrochemical water splitting. Adv. Mater. **23**(44), 5243–5249 (2011). doi:10.1002/adma.201101368

21. F.E. Osterloh, Inorganic nanostructures for photoelectrochemical and photocatalytic water splitting. Chem. Soc. Rev. **42**(6), 2294–2320 (2013). doi:10.1039/c2cs35266d

22. R. Franking, L.S. Li, M.A. Lukowski, F. Meng, Y.Z. Tan, R.J. Hamers, S. Jin, Facile post-growth doping of nanostructured hematite photoanodes for enhanced photoelectrochemical water oxidation. Energy Environ. Sci. **6**(2), 500–512 (2013). doi:10.1039/c2ee23837c

23. D.K. Zhong, J.W. Sun, H. Inumaru, D.R. Gamelin, Solar water oxidation by composite catalyst/alpha-Fe_2O_3 photoanodes. J. Am. Chem. Soc. **131**(17), 6086–6087 (2009). doi:10.1021/ja9016478

24. L.P. Zhu, L.L. Wang, N.C. Bing, C. Huang, L.J. Wang, G.H. Liao, Porous fluorine-doped gamma-Fe_2O_3 hollow spheres: synthesis, growth mechanism, and their application in photocatalysis.

ACS Appl. Mater. Interfaces **5**(23), 12478–12487 (2013). doi:10.1021/am403720r

25. D.L. Guo, H. Huang, J.Y. Xu, H.L. Jiang, H. Liu, Efficient iron-catalyzed *N*-arylation of aryl halides with amines. Org. Lett. **10**(20), 4513–4516 (2008). doi:10.1021/ol801784a

26. Y. Hou, Z.H. Wen, S.M. Cui, X.R. Guo, J.H. Chen, Constructing 2D porous graphitic C_3N_4 nanosheets/nitrogen-doped graphene/layered MoS_2 ternary nanojunction with enhanced photoelectrochemical activity. Adv. Mater. **25**(43), 6291–6297 (2013). doi:10.1002/adma.201303116

27. Q. Dong, S. Yin, C.S. Guo, X.Y. Wu, N. Kumada, T. Takei, A. Miura, Y. Yonesaki, T. Sato, Single-crystalline porous NiO nanosheets prepared from beta-$Ni(OH)_2$ nanosheets: magnetic property and photocatalytic activity. Appl. Catal. B-Environ. **147**, 741–747 (2014). doi:10.1016/j.apcatb.2013.10.007

28. G. Rothenberger, J. Moser, M. Gratzël, N. Serpone, D.K. Sharma, Charge carrier trapping and recombination dynamics in small semiconductor particles. J. Am. Chem. Soc. **107**(26), 8054–8059 (1985). doi:10.1021/ja00312a043

29. J. Zhang, J.G. Yu, Y.M. Zhang, Q. Li, J.R. Gong, Visible light photocatalytic H_2 production activity of CuS/ZnS porous nanosheets based on photoinduced interfacial charge transfer. Nano Lett. **11**(11), 4774–4779 (2011). doi:10.1021/nl202587b

30. Y.F. Yu, J. Zhang, X. Wu, W.W. Zhao, B. Zhang, Nanoporous single-crystal-Like $CdxZn_{1-x}S$ nanosheets fabricated by the cation-exchange reaction of inorganic-organic hybrid ZnS-amine with cadmium ions. Angew. Chem. Int. Ed. **51**(4), 897–900 (2011). doi:10.1002/anie.201105786

31. Z.C. Wang, Z.Y. Li, C.J. Medforth, J.H. Shelnutt, Self-assembly and self-metallization of porphyrin nanosheets. J. Am. Chem. Soc. **129**(9), 2440–2441 (2007). doi:10.1021/ja068250o

32. Y. Chen, K. Li, W. Lu, S.S.Y. Chui, C.W. Ma, C.M. Che, Photoresponsive supramolecular organometallic nanosheets induced by Pt-II•••Pt-II and C-H•••π interactions. Angew. Chem. Int. Ed. **48**(52), 9909–9913 (2009). doi:10.1002/anie.200905678

33. T. Bauer, Z.K. Zheng, A. Renn, R. Enning, A. Stemmer, J. Sakamoto, A.D. Schluter, Synthesis of free-standing, monolayered organometallic sheets at the air/water interface. Angew. Chem. Int. Ed. **50**(34), 7879–7884 (2011). doi:10.1002/anie.201100669

34. S.M. Zhou, D.K. Ma, P. Cai, W. Chen, S.M. Huang, TiO_2/$Bi_2(BDC)_3$/BiOCl nanoparticles decorated ultrathin nanosheets with excellent photocatalytic reaction activity and selectivity. Mater. Res. Bull. **60**, 64–71 (2014). doi:10.1016/j.materresbull.2014.08.023

35. N. Myung, S. Ham, S. Choi, W.G. Kim, Y.J. Jeon, K.J. Paeng, W. Chanmanee, N.R. Tacconi, K. Rajeshwar, Tailoring interfaces for electrochemical synthesis of semiconductor films: $BiVO_4$, Bi_2O_3, or composites. J. Phys. Chem. C **115**(15), 7793–7800 (2011). doi:10.1021/jp200632f

36. A. Glisenti, Interaction of formic acid with Fe_2O_3 powders under different atmospheres: an XPS and FTIR study. J. Chem. Soc. Faraday Trans. **94**(24), 3671–3676 (1998). doi:10.1039/a806080k

37. K. Dai, Y. Yao, H. Liu, I. Mohamed, H. Chen, Q.Y. Huang, Enhancing the photocatalytic activity of lead molybdate by modifying with fullerene. J. Mol. Catal. A-Chem. **374**, 111–117 (2013). doi:10.1016/j.molcata.2013.03.027

38. Z.H. Xu, J.G. Yu, Visible-light-induced photoelectrochemical behaviors of Fe-modified TiO_2 nanotube arrays. Nanoscale **3**(8), 3138–3144 (2011). doi:10.1039/c1nr10282f

39. M. Liu, X.Q. Qiu, M. Miyauchi, K. Hashimoto, Energy-level matching of Fe(III) ions grafted at surface and doped in bulk for efficient visible-light photocatalysts. J. Am. Chem. Soc. **135**(27), 10064–10072 (2013). doi:10.1021/ja401541k

40. Y. Shi, H.Y. Li, L. Wang, W. Shen, H.Z. Chen, Novel alpha-Fe_2O_3/CdS cornlike nanorods with enhanced photocatalytic performance. ACS Appl. Mater. Interfaces **4**(9), 4800–4806 (2012). doi:10.1021/am3011516

41. G.K. Pradhan, D.K. Padhi, K.M. Parida, Fabrication of alpha-Fe_2O_3 nanorod/RGO composite: a novel hybrid photocatalyst for phenol degradation. ACS Appl. Mater. Interfaces **5**(18), 9101–9110 (2013). doi:10.1021/am402487h

42. N. Liang, J.T. Zai, M. Xu, Q. Zhu, X. Wei, X.F. Qian, Novel Bi_2S_3/$Bi_2O_2CO_3$ heterojunction photocatalysts with enhanced visible light responsive activity and wastewater treatment. J. Mater. Chem. A **2**, 4208–4216 (2014). doi:10.1039/c3ta13931j

43. H.F. Cheng, B.B. Huang, X.Y. Qin, X.Y. Zhang, Y. Dai, A controlled anion exchange strategy to synthesize Bi_2S_3 nanocrystals/BiOCl hybrid architectures with efficient visible light photoactivity. Chem. Commun. **48**, 97–99 (2012). doi:10.1039/c1cc15487g

44. P. Madhusudan, J.R. Ran, J. Zhang, J.G. Yu, G. Liu, Novel urea assisted hydrothermal synthesis of hierarchical $BiVO_4$/$Bi_2O_2CO_3$ nanocomposites with enhanced visible-light photocatalytic activity. Appl. Catal. B **110**, 286–295 (2011). doi:10.1016/j.apcatb.2011.09.014

45. N. Liang, M. Wang, L. Jin, S.S. Huang, W.L. Chen, MXuQQ He, J.T. Zai, N.H. Fang, X.F. Qian, Highly efficient Ag_2O/$Bi_2O_2CO_3$ p-n heterojunction photocatalysts with improved visible-light responsive activity. ACS Appl. Mater. Interfaces **6**(14), 11698–11705 (2014). doi:10.1021/am502481z

46. M.F. Al-Kuhaili, M. Saleem, S.M.A. Durrani, Optical properties of iron oxide (alpha-Fe_2O_3) thin films deposited by the reactive evaporation of iron. J. Alloys Compd. **521**, 178–182 (2012). doi:10.1016/j.jallcom.2012.01.115

47. Q.J. Xiang, J.G. Yu, M. Jaroniec, Synergetic effect of MoS_2 and graphene as cocatalysts for enhanced photocatalytic H_2 production activity of TiO_2 nanoparticles. J. Am. Chem. Soc. **134**(15), 6575–6578 (2012). doi:10.1021/ja302846n

48. G.C. Xie, K. Zhang, B.D. Guo, Q. Liu, L. Fang, J.R. Gong, Graphene-based materials for hydrogen generation from light-driven water splitting. Adv. Mater. **25**(28), 3820–3839 (2013). doi:10.1002/adma.201301207

49. Y.B. Li, L. Zhang, A. Torres-Pardo, J.M. Gozalez-Calbet, Y.H. Ma, P. Oleynikov, O. Terasaki, S. Asahina, M. Shima, D. Cha, L. Zhao, K. Takanabe, J. Kubota, K. Domen, Cobalt phosphate-modified barium-doped tantalum nitride nanorod photoanode with 1.5% solar energy conversion efficiency. Nat. Commun. **4**, 2566 (2013). doi:10.1038/ncomms3566

50. M.C. Long, W.M. Cai, J. Cai, B.X. Zhou, X.Y. Chai, Y.H. Wu, Efficient photocatalytic degradation of phenol over Co_3O_4/$BiVO_4$ composite under visible light irradiation. J. Phys. Chem. B **110**(41), 20211–20216 (2006). doi:10.1021/jp063441z